A&A 663, A127 (2022)
https://doi.org/10.1051/0004-6361/202243115

Astronomy & Astrophysics

Growth of a filament channel by intermittent small-scale magnetic reconnection★

H. T. Li[1,3], X. Cheng[1,2,3], J. H. Guo[1,3], X. L. Yan[4], L. F. Wang[1,3], Z. Zhong[1,3], C. Li[1,3], and M. D. Ding[1,3]

[1] School of Astronomy and Space Science, Nanjing University, Nanjing 210023, PR China
e-mail: xincheng@nju.edu.cn
[2] Max Planck Institute for Solar System Research, Gottingen 37077, Germany
[3] Key Laboratory of Modern Astronomy and Astrophysics (Nanjing University), Ministry of Education, Nanjing 210023, PR China
[4] Yunnan Observatories, Chinese Academy of Sciences, Kunming 650216, PR China

Received 14 January 2022 / Accepted 15 March 2022

ABSTRACT

Context. A filament channel (FC), a plasma volume where the magnetic field is primarily aligned with the polarity inversion line, is believed to be the pre-eruptive configuration of coronal mass ejections. Nevertheless, evidence for how the FC is formed is still elusive.

Aims. In this paper, we present a detailed study of the build-up of a FC in order to understand its formation mechanism.

Methods. The New Vacuum Solar Telescope (NVST) of the Yunnan Observatory and the Optical and Near-infrared Solar Eruption Tracer (ONSET) of Nanjing University, as well as the Atmospheric Imaging Assembly (AIA) and Helioseismic and Magnetic Imager (HMI) on board the Solar Dynamics Observatory (SDO), are used to study the growth process of the FC. Furthermore, we reconstruct the nonlinear force-free field (NLFFF) of the active region using the regularized Biot-Savart laws (RBSL) and the magnetofrictional method to reveal the three-dimensional (3D) magnetic field properties of the FC.

Results. We find that partial filament materials are quickly transferred to longer magnetic field lines formed by small-scale magnetic reconnection, as evidenced by dot-like Hα and extreme ultraviolet (EUV) brightenings and subsequent bidirectional outflow jets, as well as untwisting motions. The Hα and EUV bursts appear repeatedly at the same location and are closely associated with flux cancelation, which occurs between two small-scale opposite polarities and is driven by shearing and converging motions. The 3D NLFFF model reveals that the reconnection takes place in a hyperbolic flux tube that is located above the flux-cancelation site and below the FC.

Conclusions. The FC is gradually built up toward a twisted flux rope via a series of small-scale reconnection events that occur intermittently prior to the eruption.

Key words. Sun: activity – Sun: filaments, prominences – Sun: magnetic fields

1. Introduction

Coronal mass ejections (CMEs) are large-scale explosive phenomena in the solar system that can give rise to severe space weather events (Chen 2011). A promising method to forecast the occurrence of CMEs is to monitor their pre-eruptive configurations, including filaments, coronal cavities, sigmoids, and hot channels (Low & Hundhausen 1995; Hudson & Lemen 1998; Wang & Stenborg 2010; Zhang et al. 2012; Cheng et al. 2013, 2014; Huang et al. 2019). These pre-eruptive structures can be regarded as different manifestations of a common configuration, namely the so-called filament channels (FCs), at different evolutionary stages and/or in different plasma environments as suggested by a recent review paper by Patsourakos et al. (2020).

Observationally, a FC corresponds to a plasma volume where the magnetic field is primarily aligned with the polarity inversion line (PIL). The magnetic field within the FC is often seen to be highly sheared or twisted, which can be classified into two categories: sheared magnetic arcade (SMA; Kippenhahn & Schlüter 1957; Antiochos et al. 1994; DeVore & Antiochos 2000) and magnetic flux rope (MFR; Kuperus & Raadu 1974; Wang et al. 1996; Aulanier et al. 1998; Gibson & Fan 2006; Cheng et al. 2014; Yan et al. 2015). The latter is usually believed to be more coherent and has a larger average twist (e.g., ≥1 turn). In many cases, the pre-eruptive FC manifests as a filament on the solar disk or prominence above the solar limb with cool material suspended at magnetic dips (Tandberg-Hanssen 1974; Antiochos et al. 1994; Martin 1998; Mackay et al. 2010; Chen et al. 2014; Mackay 2015). However, this is not always the case, as some studies have shown that magnetic dips are not necessary and the filament threads are simply observational manifestations of dynamical counter-streaming flows (Karpen et al. 2001; Zou et al. 2016, 2017; Guo et al. 2021b).

At present, the mechanism by which FCs are formed is still hotly debated. Many models have been proposed to interpret the formation of FCs, including the flux emergence model (Okamoto et al. 2008; Cheung & Isobe 2014; Chintzoglou et al. 2019), the flux cancelation model (Martin et al. 1985; van Ballegooijen & Martens 1989; van Ballegooijen et al. 2000; Gaizauskas et al. 2001; Kumar et al. 2015; Yang et al. 2016a), and the helicity condensation model (Alexakis et al. 2006; Török et al. 2010; Antiochos 2013). The emergence model assumes a highly twisted flux rope existing in the convective zone that partially emerges to the corona via magnetic buoyancy. The emerging flux then forms an MFR through magnetic

★ Movie associated to Fig. 3 is available at https://www.aanda.org

reconnection driven by shearing and converging flows (Syntelis et al. 2017; Toriumi & Takasao 2017). In the flux cancelation model, the initial configuration is assumed to be a potential field. As the shearing motion along the PIL and converging flows toward the PIL are introduced, the potential field lines are first sheared and then reconnected to form two groups of new fluxes, one of which becomes longer and more twisted and the other is shorter and close to the potential. Afterwards, the short flux submerges to below the photosphere, appearing as flux cancelation (van Ballegooijen & Martens 1989). Obviously, in the two models, the sheared field and magnetic reconnection are two common ingredients, while the only difference is the origin of the sheared flux. However, the helicity condensation model is completely distinct from these two latter models, and is essentially an accumulation of magnetic shear through an inverse helicity cascade, during which helicity is injected into the coronal flux by photospheric motions and flux emergence and submergence (Török et al. 2010; Antiochos 2013).

Flux cancelation is found to be prevalent during the formation of the pre-eruptive MFR (e.g., Wang & Muglach 2007; Mackay et al. 2008; Chintzoglou et al. 2019). Okamoto et al. (2008, 2009) studied a sequence of vector magnetograms and found that the region with adjacent opposite polarities – where the horizontal magnetic field is strong but the vertical field is weak – first widens and then becomes narrow. Meanwhile, the reversal of the direction of the horizontal field along the PIL, the blueshift of spectral lines, and diverging flows are observed. These latter authors argued that these features are strong evidence in favor of the MFR emergence model. However, such an interpretation was subsequently challenged by Vargas Domínguez et al. (2012), who pointed out that the flux cancelation model is also able to give rise to the same observational features. Recently, it was revealed that small-scale flux cancelation is even more common than previously thought, and that may even drive nanoflares to heat the chromosphere and corona (Chitta et al. 2018; Li et al. 2018; Priest et al. 2018).

In this paper, we study the growth of an active region (AR) NOAA 12790 FC with Hα images of high spatial and temporal resolution. Our most interesting finding is that the FC is gradually built up by a number of small-scale reconnection events occurring intermittently above the flux cancelation site prior to the eruption, at least during the time period we studied. Importantly, this significantly bolsters a previous argument that the pre-eruptive MFR can be quickly formed by preceding confined major flares (Patsourakos et al. 2013; Liu et al. 2018). Section 2 describes the instruments we used. The main results are presented in Sect. 3, followed by a summary and discussions in Sect. 4.

2. Instruments

The FC we study was primarily observed by the 1 m New Vacuum Solar Telescope (NVST; Liu et al. 2014; Yan et al. 2020b), which is located at Fuxian Lake in the Yunnan Province and is operated by the Yunnan Observatory. The NVST is designed to observe the fine structures in the lower solar atmosphere and reveal the origin and mechanism of solar activities with high spatial (~0.165″ per pixel) and temporal resolution (~12 s). Due to its limited field of view (FOV; ~3′), the NVST can only observe part of the FC. Fortunately, the Optical and Near-Infrared Solar Eruption Tracer (ONSET; Fang et al. 2012, 2013; Cheng et al. 2015), also located at Fuxian Lake, has a larger FOV and therefore enables us to observe the entire FC. Moreover, we also use data from the Atmospheric Imaging Assembly (AIA; Lemen et al. 2012) on board the Solar Dynamics Observatory (SDO; Pesnell et al. 2012), which provides full solar disk images in seven extreme ultraviolet (EUV) and two ultraviolet (UV) passbands. The temporal cadence is 12 s (24 s) for the EUV (UV) passbands. The pixel size is 0.6″ for both. The Helioseismic and Magnetic Imager (HMI; Schou et al. 2012; Scherrer et al. 2012) on board SDO provides line-of-sight (temporal resolution ~45 s) and vector magnetograms (temporal resolution ~12 min), which are used to investigate the temporal variation in magnetic flux and reconstruct the three-dimensional (3D) coronal magnetic field, respectively.

3. Results

3.1. Growth of filament channels and mass transfer

On 2020 Dec. 07, the filament originating from AR 12790 produced the first halo CME in the 25th solar cycle, as shown in Fig. 1a (also see Yan et al. 2021). Prior to the eruption, the filament threads are highly sheared and the corresponding magnetic configuration, defined as the FC, is expected to be mainly aligned with the main PIL of the photospheric magnetic field (the gold line in Fig. 1b), which is composed of a leading negative polarity and some dispersed positive polarities. After the major eruption, a partial FC remains south of the PIL, and manifests as sheared filament threads (Fig. 1c). During the following time period of more than 40 h, the FC seems to continuously grow and finally appears as a well-observed filament on 2020 Dec. 10. At approximately 03:50 UT, the FC erupts again but a full eruption is not seen (Fig. 1d), only an A-class flare.

In this paper, we mainly focus on one episode of the FC build-up after the first major eruption, because it happens to have been simultaneously observed by the NVST and ONSET. At 05:00 UT on 2020 Dec. 08, an Hα burst appears as a small-scale brightening near the north end of the filament. Afterward, some new filament threads are formed with their northern ends extending to the penumbra of the preceding sunspot at 05:52 UT (Fig. 2b). The small-scale Hα burst, as well as the accompanied dynamics of the filament threads, also cause a response at the AIA EUV passbands (Fig. 2a). As shown in Fig. 2c, with the beginning of the EUV brightening, one can see that partial filament materials (the dotted line in Fig. 2c) are transferred from the southern to the northern part of the main PIL. At 05:44 UT, some continuous and long filament threads clearly appear at the AIA 304 Å passband, highly resembling what is observed in Hα. It is also apparently observed from the running-difference images as shown in Fig. 2d. During the same time period, some heated plasma blobs are also observed to be quickly ejected from the brightening site along two opposite directions parallel to the PIL, suggestive of the occurrence of magnetic reconnection.

Despite the limited FOV of the NVST, it covered the Hα and EUV burst in its entirety. From the Hα images of high spatio-temporal resolution (Figs. 3a–c) and the attached movie, one can clearly observe the transfer of the filament materials from arc-shaped arcades to the north part of the PIL following the brightening. Before and during the transfer process, the southern arc-shaped filament is even found to present an untwisting motion. The rotation direction is clockwise when observed from the south of the AR, indicating that the magnetic structure of the southern arc-filament reserves a certain amount of twist, at least being highly sheared, as suggested by Wang et al. (2015). The corresponding chirality is sinistral, or the helicity is positive, which is consistent with the hemispheric rule of

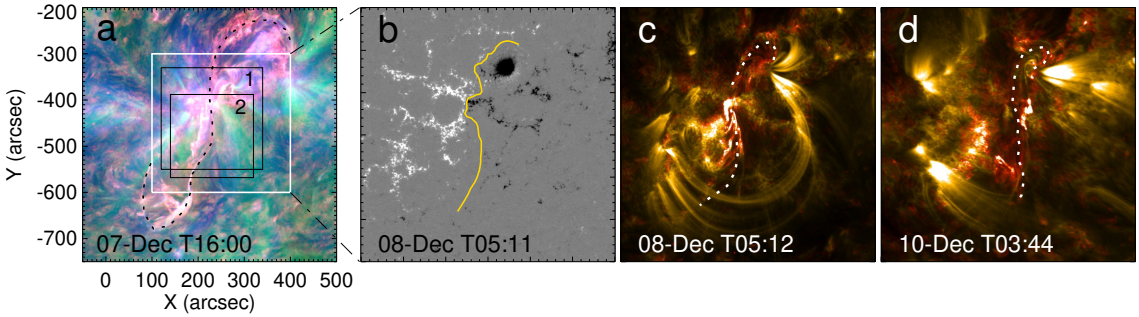

Fig. 1. FC at different evolutionary stages. *Panel a*: composite of the AIA 304 Å, 211 Å, and 171 Å images showing the filament eruption on 2020 Dec. 7. The white box shows the FOV of *panels b–d*. The black boxes 1 and 2 show the FOVs of the ONSET and NVST images as shown in Figs. 2b and 3, respectively. *Panel b*: HMI line-of-sight magnetogram with the main PIL indicated by the gold line. *Panels c–d*: composite of the AIA 304 Å and 171 Å images showing the remained FC and the confined filament eruption. The dashed line indicate the corresponding FC at different instants.

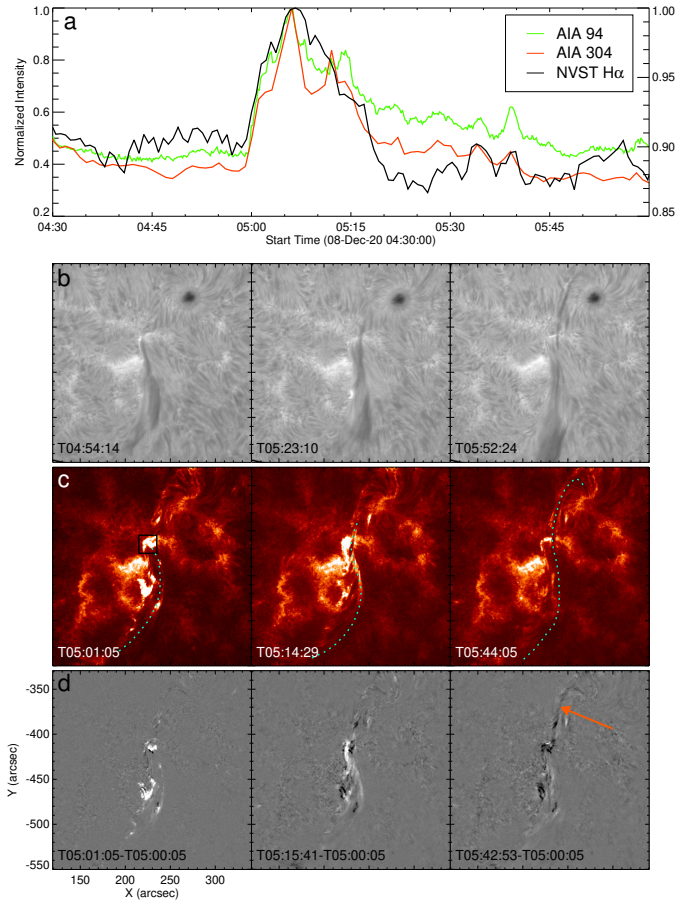

Fig. 2. Evolution of the FC in Hα and EUV waves. *Panel a*: temporal evolution of the normalized AIA 94 Å, 304 Å, and Hα intensities within the black box in *panel c*. *Panel b*: ONSET Hα images showing the formation of the filament threads. They are aligned with the AIA images through cross-correlation between the ONSET and HMI white-light images. *Panels c and d*: AIA 304 Å and corresponding running-difference images. The dashed line represents the filament threads, and the orange arrow points out the transferred filament.

magnetic helicity (Martin et al. 1992; Martin 1998; Chen et al. 2014; Ouyang et al. 2017). We propose that in this instance the reconnection most likely takes place between the arc-shaped filament system and the nearby flux above the northern PIL. It forms longer magnetic field lines, almost spanning the entire PIL, and gives rise to the Hα and EUV burst at the same time. As the long field lines are filled with transferred filament materials, they then become visible as dark threads.

The Hα off-band observations of the NVST provided Doppler shift maps during the formation of the FC. For this particular event, the wavelengths of Hα off-band were centered at 6562.8 ± 0.4 Å. The formula we used to calculate Doppler maps was from Langangen et al. (2008):

$$D = \frac{B - R}{B + R}, \tag{1}$$

where B and R represent the blue-wing and red-wing intensities, respectively. The results are shown in Figs. 3d–f, from which we can see that the counter-streaming along the arc-shaped FC instantly becomes visible once the Hα/EUV brightenings appear. However, shortly afterwards, the blueshift starts to dominate (Figs. 3e–f), which is a result of the combination of the untwisting motion of the filament magnetic structures and the field-aligned motion of the materials from the leg to top of the field lines. The latter is most likely driven by the reconnection outflows.

To quantify the motion of the bidirected outflows ejected by magnetic reconnection in the plane of sky, we took two curved slices AB and CD along the FC as shown in Figs. 4a and c. The slice-time plots for the AIA 304 Å and NVST Hα passbands are displayed in Figs. 4b and d, respectively. We clearly see two groups of outflow jets that are launched after the appearance of the brightenings and then quickly move in opposite directions. At the AIA passbands, the outflow jets are only visible at the 304 Å passband, inferring that they are not heated to the coronal temperatures (e.g., above 1 MK). Through tracking the trajectories of the outflows, we estimated the velocities to be in the range of 100−150 km s^{-1}. Similar to the AIA 304 Å passband, at the Hα passband, we observe some quickly moving dark jets, while the corresponding velocities are slightly lower.

3.2. Causes and intermittency of magnetic reconnection

We speculate that the formation of the FC prior to the eruption may experience multiple reconnection episodes. That is to say, a single reconnection event, as revealed by the Hα/EUV burst, may not be able to supply enough magnetic flux to trigger the eruption (e.g., Zhang et al. 2014; Xing et al. 2020). Through inspecting the long-term evolution of the AIA 304 Å

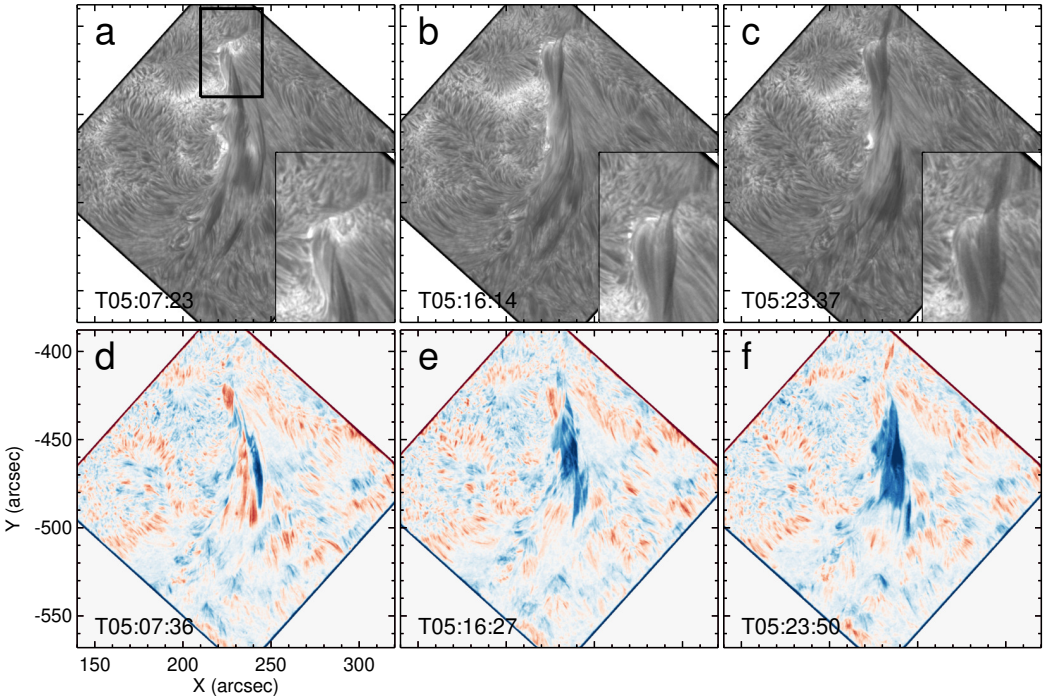

Fig. 3. Mass transfer observed by NVST. *Panels a–c*: NVST Hα images showing FC evolution and growth to the northern part. A zoom into the region of interest is shown in the lower right corner of each panel (an animation is available online). *Panels d–f*: corresponding pseudo Doppler maps.

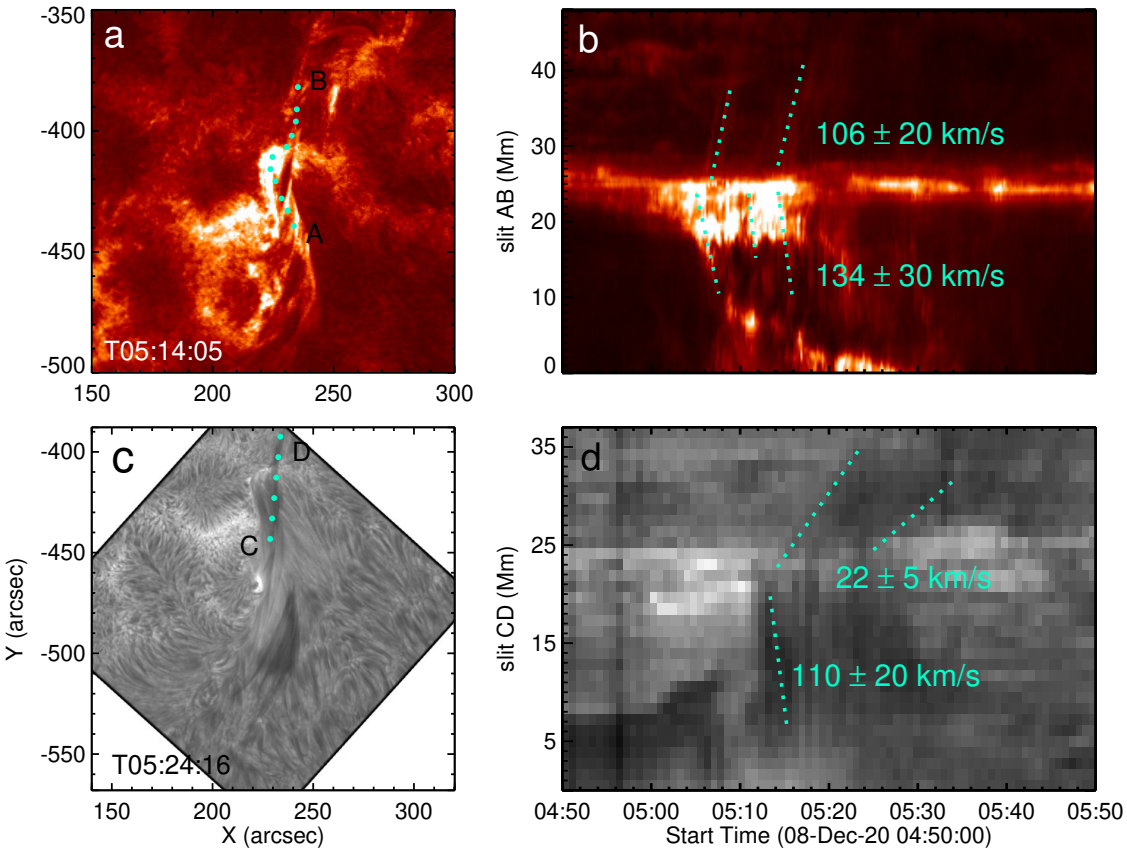

Fig. 4. Time–distance diagrams showing the outflow jets. *Panels a and c*: AIA 304 Å and NVST Hα images. The curved slits AB and CD, as shown by two dotted lines, represent the directions of the reconnection outflows. *Panels b and d*: 304 Å and Hα slice-time plots. The inclined dotted lines show the trajectories of outflow jets.

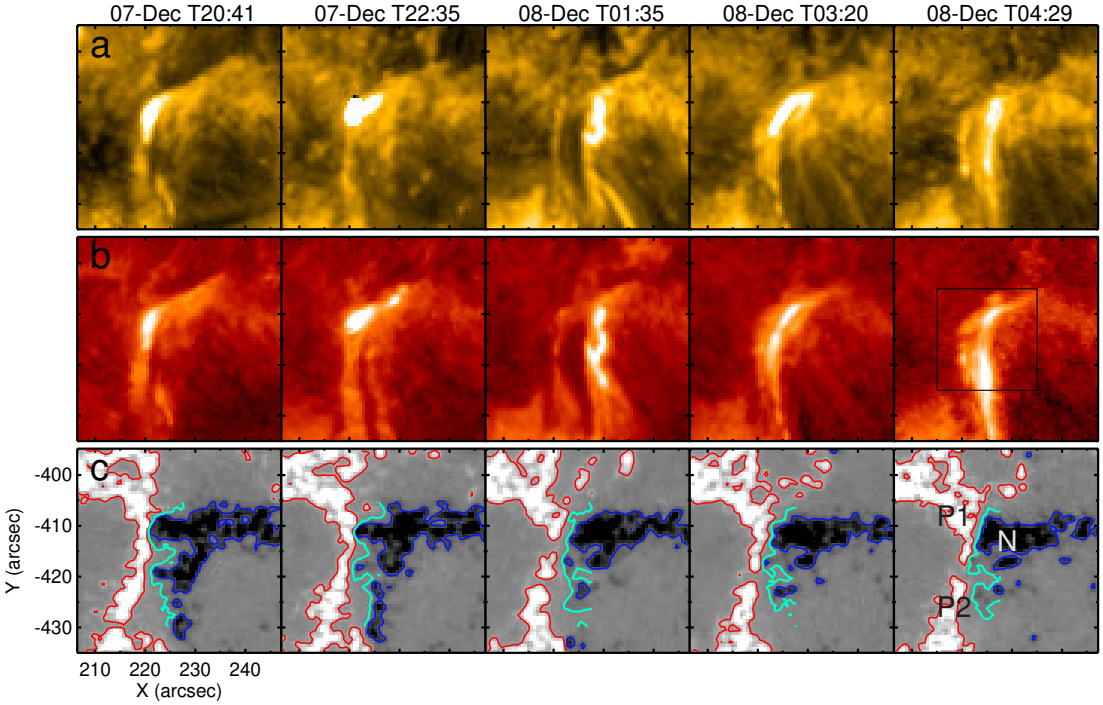

Fig. 5. Intermittent brightenings observed by the AIA. *Panels a and b*: time-sequence of AIA 171 Å and 304 Å images displaying repeatedly occurred EUV bursts at the site of the flux cancelation. The black box shows the region for integrating the intensity. *Panel c*: HMI LOS magnetograms with red/blue contours representing the positive/negative magnetic fields of ±100 G. The cyan line represents the PIL, and P1 (P2) and N represent the positive and negative polarities, respectively.

and 171 Å images, we find at least nine EUV bursts appearing at the same location repeatedly and presenting a similar morphology, as shown in Figs. 5a and b. Each of them lasts for about 10 min, although their magnitudes change from case to case, as shown by the evolutions of the 304 Å and 171 Å intensities (Fig. 6b). This implies that the formation of a full-fledged FC needs to experience multiple reconnection processes, which take place intermittently and manifest as the intermittent appearance of EUV bursts.

The Hα/EUV burst is found to be driven by the shearing and converging flows at the photosphere. Figure 5c shows a time-sequence of the HMI line-of-sight magnetograms. We find that the EUV bursts are most likely related to the interaction of two parasitic positive and negative polarities. To confirm such an interaction, we inspected the distribution and evolution of the velocity field in the photosphere, which we estimated using the HMI SHARP data and the DAVE4VM method proposed by Schuck (2008). It is clear that, in such a small-scale region, the negative polarities (N) are continuously moving toward to the positive ones (P1, P2) with a maximum velocity of 0.5 km s^{-1} (Fig. 6a). At the location of the Hα/EUV burst, they ceaselessly cancel each other and give rise to Hα and EUV bursts. The flux cancelation is also revealed by the integrated negative flux, which shows a gradual decrease over time, as shown by the black curve in Fig. 6b. We estimate the total canceled negative flux during 12 h to be about 5×10^{17} Mx, with an average cancelation rate of $\sim 10^{13}$ Mx s^{-1}. Comparing with the flux cancelation rate derived by Díaz Baso et al. (2021), the rate derived here seems to be insufficient for a strong reconnection event. At the same time, the positive flux also tends to decrease in general, but increases during two intervals (the blue curve in Fig. 6b). The increase in flux is mainly caused by the adjacent positive polarity continuously flowing into the region where we integrate the flux.

3.3. Three-dimensional magnetic properties of filament-channel build-up

To understand the 3D magnetic properties of the FC observed here, we reconstructed the coronal magnetic field of the source region based on the nonlinear force-free field (NLFFF) assumption using the HMI photospheric vector magnetogram as the bottom boundary (Yan et al. 2001; Canou et al. 2009; Wiegelmann & Sakurai 2012; Yang et al. 2016b; Zhong et al. 2019; Qiu et al. 2020). We first tried the extrapolation method (Guo et al. 2010; Zhu et al. 2016) and found that it is difficult to reproduce the magnetic field comparable with the morphology of the observed filament threads. We then resorted to the magnetic flux rope (MFR) embedding method based on regularized Biot-Savart laws (RBSL; Titov et al. 2014, 2018; Guo et al. 2019). The procedure was divided into four steps. First, we took advantage of the 304 Å images at 05:24 UT to derive the path of the FC, as shown in Fig. 7a. According to previous statistics (Tandberg-Hanssen 1995; Filippov & Den 2000; Engvold 2015), the height of active region filaments ranges from 5 Mm to 30 Mm. We therefore set the height of the MFR axis to 30 Mm and the MFR minor radius to 25 Mm, assuming that the lower half of the MFR is fully filled by cool material. The 3D path of the MFR was estimated according to Guo et al. (2021a). Second, we calculated a potential field utilizing the normal magnetic field component, where the projection effect was corrected (Wiegelmann et al. 2006; Guo et al. 2017). Third, we set the physical parameters of the RBSL model including the average value of unsigned magnetic flux at the two MFR footprints (1.72×10^{21} Mx) and the strength of the electric current following Eq. (12) in Titov et al. (2018). Finally, we inserted the MFR derived by the RBSL model into the potential field along the path of the FC and then performed a relaxation using the magnetofrictional code (Guo et al. 2016a,b). After relaxation, the

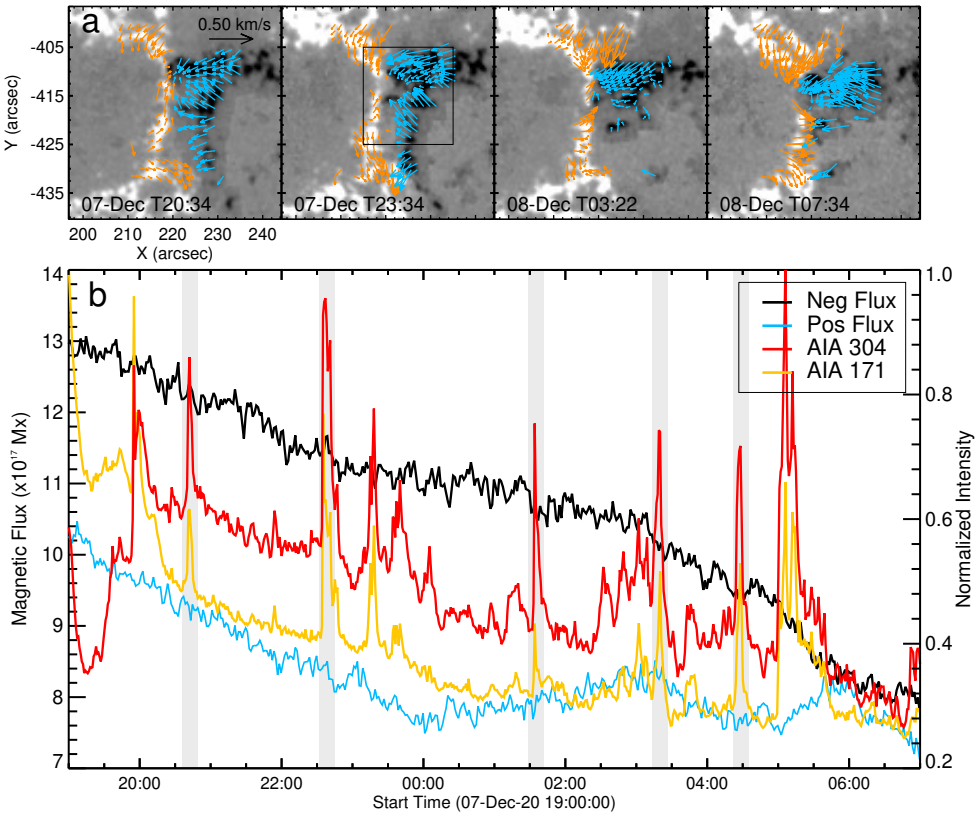

Fig. 6. Evolution of the magnetic fileds. *Panel a*: HMI LOS magnetograms superimposed over the velocity fields. The blue (orange) arrows represent the velocity of the negative (positive) polarities. *Panel b*: temporal evolution of integrated magnetic fluxes and normalized 304 Å and 171 Å intensities. The black box shows the region for integrating magnetic fluxes. The shadowed regions correspond to the time periods of bursts shown in Fig. 5.

force-free metric was $\sigma_J = 0.28$, and the divergence-free metric was $\langle |f_i| \rangle = 1.47 \times 10^{-4}$, which were sufficiently small and generally acceptable according to Guo et al. (2021a)[1].

Figure 7b shows selected magnetic field lines of the NLFFF structure, from which one can see that there exist two groups of highly sheared field lines underneath the modeled MFR (M1) as indicated by L1 and L2 in Fig. 7c. The right leg of L1 and the left leg of L2 form an X-shaped configuration. Their footpoints are both rooted in the region where the converging motion and flux cancelation takes place. At the same time, we also observed some much shorter loops located below the X-shaped configuration (M2 in Fig. 7c). Such a configuration is consistent with the tether-cutting reconnection model (Moore et al. 1980, 2001), in which the reconnection of two sheared arcades forms a longer and twisted loop above and a shorter semicircular-like loop below. Owing to the magnetic tension, the flux M1 rises up. Because the southern part of M1 is highly inclined, the reconnection outflows toward the south also produce an upward velocity, appearing as the blueshifts in the NVST off-band images. Meanwhile, the northern part is low-lying, and the outflows toward the north appear as redshifts at the location near [240, −400]. On the other hand, due to the downward magnetic tension, M2 submerges, which manifests as flux cancelation.

To further quantify the property of the reconnection, we calculated the squashing factor (Q) and the current density on the plane almost perpendicular to the inserted MFR axis and cutting through the reconnection X-point as shown in Figs. 7d and e. The isosurfaces of high Q values indicate quasi-separatrix layers (QSLs), which describe the locations of rapid magnetic connectivity changes (Priest & Démoulin 1995; Titov et al. 2002). We find that the MFR we see in the observations studied here is well wrapped by the QSLs and that an obvious hyperbolic flux tube (HFT) is formed below the MFR. We also find the current density to be the strongest at the HFT. These features strengthen our previous conjecture as to the occurrence of magnetic reconnection. However, it is worth mentioning that the height of the reconnection X-point (about 12 Mm) in the NLFFF structure is subject to large uncertainty. This may be caused by the NLFFF assumption, which did not consider the chromosphere and transition region that may include a strong Lorenz force. Second, the parameters of the inserted MFR were set by experience. When we changed the height and radius of the MFR by ±5 Mm, the height of reconnection site varied from 5 to 18 Mm. Fortunately, the AR was also observed by IRIS, the spectroscopic data of which allowed us to further explore the properties of the reconnection responsible for the FC formation, in particular its height. The results will be presented in a separate paper. Moreover, we find that the derived MFR transits to an SMA during the relaxation if the average twist of the inserted MFR is turned down. However, the reconnection between two sheared arcades is still observed.

To strengthen our argument that the FC is gradually built up by the multiple reconnection events that occur intermittently, we compared the two NLFFF configurations before and after the intermittent reconnection events we observed. For the two configurations, all initial input values are the same except for the bottom magnetic field. To uncover the temporal variation of the FC, we needed to calculate the twist and toroidal flux of the MFR. We first identified the boundary of the MFR (Fig. 7e) by using the IDL routine *region_grow.pro*[2]. This method searches for an MFR region starting from a selected small region near the MFR center and determining which neighbor pixels should be added

[1] https://github.com/njuguoyang/magnetic_modeling_codes.

[2] https://www.l3harrisgeospatial.com/docs/REGION_GROW.html.

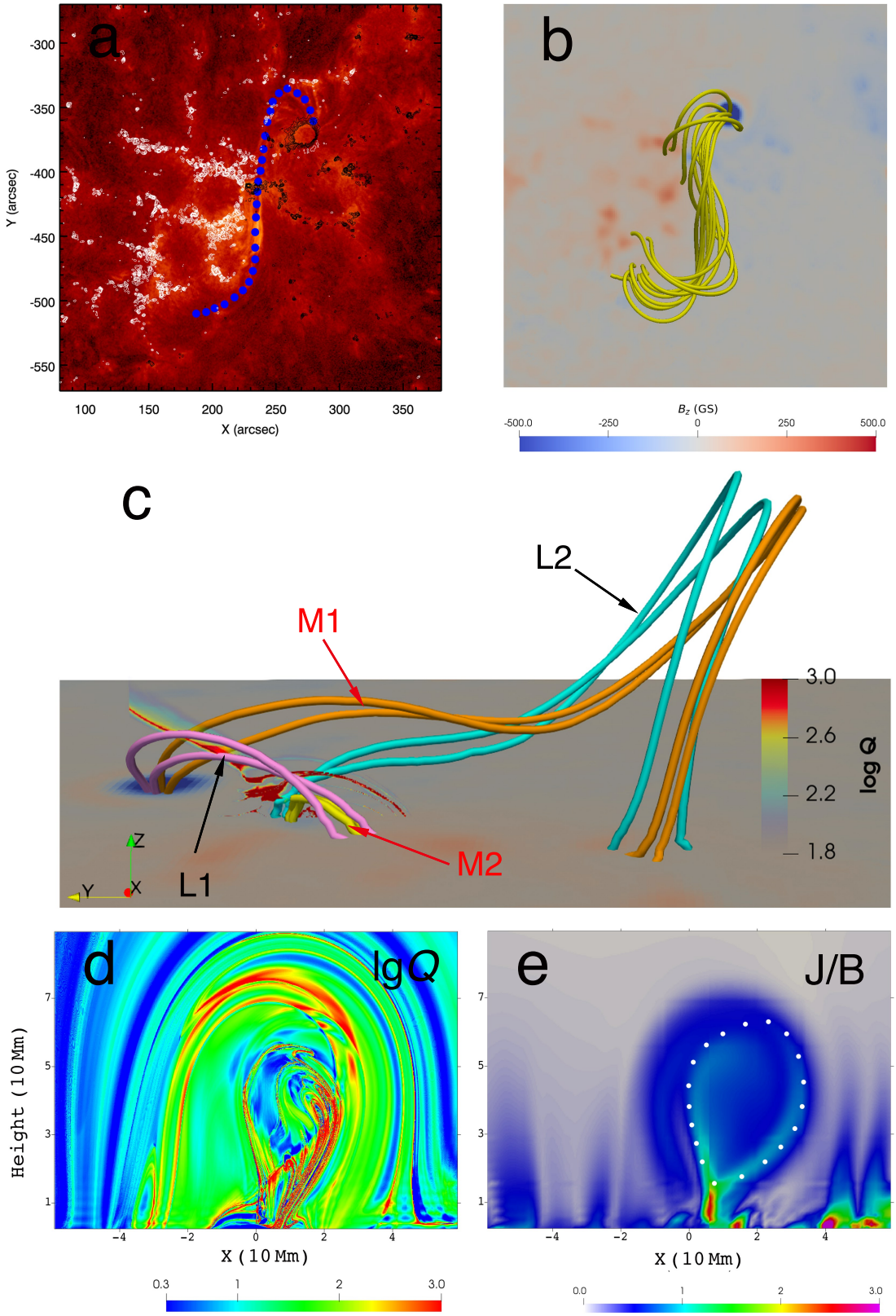

Fig. 7. 3D magnetic configuration of the FC. *Panel a*: AIA 304 Å image with the dotted curve overlaid showing the path of the FC. *Panel b*: collection of 3D magnetic field lines indicating the MFR as seen from the top. The bottom boundary is the HMI LOS magnetogram. *Panel c*: side view of *panel b* coupled with Q values. L1 and L2 delineate two groups of sheared arcades, and M1 and M2 represent the MFR field lines and small flare loops, respectively. The coordinates x, y, and z represent west, north, and altitude. *Panel d*: distribution of Q values on the plane perpendicular to the MFR axis, as pointed out by the dashed line in *panel b*. *Panel e*: distribution of J/B in the same plane and the dotted line indicates the outer boundary of the MFR.

Table 1. Average twist numbers and toroidal fluxes for the NLFFF configurations at two moments.

Time (UT)	Average twist	Toroidal flux (Mx)
07-Dec. 20:36:00	0.86 ± 0.01	$1.09 \pm 0.12 \times 10^{21}$
08-Dec. 05:12:00	0.88 ± 0.03	$1.52 \pm 0.24 \times 10^{21}$

to the region. We then adjusted the location of the small region and repeated the same procedure seven times. Finally, using the code provided by Liu et al. (2016)[3], we calculated the twist and toroidal flux of magnetic field surrounded by the identified boundary and took their averages as eventual values. The uncertainties are the corresponding standard deviations, as listed in Table 1. We find that the two values both increase during the FC growth, as we expected. Furthermore, we notice that the average twist of the MFR is smaller than one, indicating that the less twisted magnetic lines dominate the MFR. This might be the primary reason for the FC eruption being confined to 2020 Dec. 10.

4. Summary and discussion

In this paper, we study the growth of a FC in the AR NOAA 12790. We find that the FC gradually builds up by a series of small-scale reconnection events, which manifest as repeated Hα and EUV bursts. The Hα and EUV emission enhancement, bi-directional outflow jets, and untwisting motion during the observed burst provide strong evidence of magnetic reconnection. Thanks to the NVST data of high spatio-temporal resolution, we observe that the filament materials are partly and quickly transferred to longer and more twisted magnetic field lines, which are most likely formed during the burst. The NLFFF of the AR using the MFR embedding method further reveals the reconnection configuration, which is composed of two groups of SMAs and an HFT embedded in between. As the HFT reconnection occurs, the long and twisted flux is gradually accumulated, resembling the FC. This process also produces the short loops during the same period, which are subsequently submerged, appearing as the small-scale flux cancelation. The horizontal velocity field in the photosphere further discloses the driver of the HFT reconnection, that is, the continuous shearing and converging flows near the flux cancelation site.

The FC build up revealed here is in favor of the flux cancelation model proposed by van Ballegooijen & Martens (1989). In addition, we uncover two new features that were not specified in this model. The first is that the reconnection configuration is of the HFT type rather than of the bald-patch type as indicated in the model. The second and more interesting feature is that the HFT configuration and thus the HFT reconnection are intermittent rather than continuous, even though the driving flows and flux cancelation appear to be continuous. We thus suspect that the reconnection configuration is highly dynamic over time. During the nonburst periods, the reconnection is perhaps extremely weak and the corresponding configuration also changes into a bald patch, which only allows the magnetic dissipation in the photosphere, giving rise to the flux cancelation. On the other hand, we notice that the seed flux building the FC we study is from the remains of the previous eruption on 2020 Dec. 7. For a full-fledged FC, its formation may therefore be more complicated, most likely involving multiple mechanisms.

[3] http://staff.ustc.edu.cn/~rliu/qfactor.html.

The transfer of material is an important indicator of the reorganization of the magnetic field through magnetic reconnection. Such a phenomenon has been observed many times, in particular, during the eruption of filaments. Yang et al. (2019) found that, during the eruption of a mini-filament, the erupting dark threads clearly untwist at the same time as the associated blowout jets rotate in the nearby large-scale loops. These authors therefore proposed that the reconnection takes place between the filament flux and the background field and rapidly transfers magnetic twist from the former to the latter, as delineated in their Fig. 8. Such a twist transfer process may be more common during the confined or failed filament eruption for the sake of re-distributing magnetic helicity (e.g., Yan et al. 2020a,c). The event studied here further reveals that the material transfer and twist transfer also occur during the growth of the FC. For each Hα and EUV burst event, the flux injected to the FC may be very limited. However, with a number of such small-scale events during a long time period, the FC can be easily built up and ready for eruption.

Such build-up of the FC through intermittent reconnection was indicated by Guo et al. (2013). Through investigating the evolution of magnetic helicity and twist of a flare-productive active region, these authors concluded that the confined flares prior to the eruptive one play an important role in building up the eruptive MFR. The confined flares that these authors see intermittently occurring near the PIL are similar to the Hα and EUV bursts observed here, while the only difference is that the magnitude of the bursts seen here is much lower. It seems that the larger the burst magnitude is, the more the flux added to the FC (e.g., Liu et al. 2018). On the other hand, Guo et al. (2013) identified that the reconnection they observed took place in the whole QSLs that demarcated the MFR from the ambient field. However, for the current case, the reconnection is demonstrated to occur in the more localized HFT between the MFR and the flux cancelation site.

Acknowledgements. We thank the referee for his/her careful reading to improve the clarity of the manuscript. We also thank the NVST, ONSET, SDO/AIA, and SDO/HMI teams for providing the high-cadence data. This work is supported by NSFC grants 11722325, 11733003, 11790303, 11873087, Yunnan Science Foundation for Distinguished Young Scholars No. 202001AV070004 and National Key R&D Program of China under grant 2021YFA1600504. X.C. is also supported by Alexander von Humboldt foundation.

References

Alexakis, A., Mininni, P. D., & Pouquet, A. 2006, ApJ, 640, 335
Antiochos, S. K. 2013, ApJ, 772, 72
Antiochos, S. K., Dahlburg, R. B., & Klimchuk, J. A. 1994, ApJ, 420, L41
Aulanier, G., Demoulin, P., van Driel-Gesztelyi, L., Mein, P., & Deforest, C. 1998, A&A, 335, 309
Canou, A., Amari, T., Bommier, V., et al. 2009, ApJ, 693, L27
Chen, P. F. 2011, Liv. Rev. Sol. Phys., 8, 1
Chen, P. F., Harra, L. K., & Fang, C. 2014, ApJ, 784, 50
Cheng, X., Zhang, J., Ding, M. D., et al. 2013, ApJ, 769, L25
Cheng, X., Ding, M. D., Zhang, J., et al. 2014, ApJ, 789, L35
Cheng, X., Hao, Q., Ding, M. D., et al. 2015, ApJ, 809, 46
Cheung, M. C. M., & Isobe, H. 2014, Liv. Rev. Sol. Phys., 11, 3
Chintzoglou, G., Zhang, J., Cheung, M. C. M., & Kazachenko, M. 2019, ApJ, 871, 67
Chitta, L. P., Peter, H., & Solanki, S. K. 2018, A&A, 615, L9
DeVore, C. R., & Antiochos, S. K. 2000, ApJ, 539, 954
Díaz Baso, C. J., de la Cruz Rodríguez, J., & Leenaarts, J. 2021, A&A, 647, A188
Engvold, O. 2015, in Description and Classification of Prominences, eds. J. C. Vial, & O. Engvold, Astrophys. Space Sci. Lib., 415, 31
Fang, C., Chen, P. F., Ding, M. D., Dai, Y., & Li, Z. 2012, in EAS Pub. Ser., eds. M. Faurobert, C. Fang, & T. Corbard , 55, 349
Fang, C., Chen, P.-F., Li, Z., et al. 2013, Res. Astron. Astrophys., 13, 1509
Filippov, B. P., & Den, O. G. 2000, Astron. Lett., 26, 322
Gaizauskas, V., Mackay, D. H., & Harvey, K. L. 2001, ApJ, 558, 888

Gibson, S. E., & Fan, Y. 2006, J. Geophys. Res. (Space Phys.), 111, A12103
Guo, Y., Schmieder, B., Démoulin, P., et al. 2010, ApJ, 714, 343
Guo, Y., Ding, M. D., Cheng, X., Zhao, J., & Pariat, E. 2013, ApJ, 779, 157
Guo, Y., Xia, C., & Keppens, R. 2016a, ApJ, 828, 83
Guo, Y., Xia, C., Keppens, R., & Valori, G. 2016b, ApJ, 828, 82
Guo, Y., Cheng, X., & Ding, M. 2017, Sci. China Earth Sci., 60, 1408
Guo, Y., Xu, Y., Ding, M. D., et al. 2019, ApJ, 884, L1
Guo, J. H., Ni, Y. W., Qiu, Y., et al. 2021a, ApJ, 917, 81
Guo, J. H., Zhou, Y. H., Guo, Y., et al. 2021b, ApJ, 920, 131
Huang, Z. W., Cheng, X., Su, Y. N., Liu, T., & Ding, M. D. 2019, ApJ, 887, 130
Hudson, H. S., Lemen, J. R., & St. Cyr, O. C., Sterling, A. C., & Webb, D. F., 1998, Geophys. Rev. Lett., 25, 2481
Karpen, J. T., Antiochos, S. K., Hohensee, M., Klimchuk, J. A., & MacNeice, P. J. 2001, ApJ, 553, L85
Kippenhahn, R., & Schlüter, A. 1957, ZAp, 43, 36
Kumar, P., Yurchyshyn, V., Wang, H., & Cho, K.-S. 2015, ApJ, 809, 83
Kuperus, M., & Raadu, M. A. 1974, A&A, 31, 189
Langangen, Ø., Rouppe van der Voort, L., & Lin, Y. 2008, ApJ, 673, 1201
Lemen, J. R., Title, A. M., Akin, D. J., et al. 2012, Sol. Phys., 275, 17
Li, D., Li, L., & Ning, Z. 2018, MNRAS, 479, 2382
Liu, Z., Xu, J., Gu, B.-Z., et al. 2014, Res. Astron. Astrophys., 14, 705
Liu, R., Kliem, B., Titov, V. S., et al. 2016, ApJ, 818, 148
Liu, L., Cheng, X., Wang, Y., et al. 2018, ApJ, 867, L5
Low, B. C., & Hundhausen, J. R. 1995, ApJ, 443, 818
Mackay, D. H. 2015, in Formation and Large-Scale Patterns of Filament Channels and Filaments, eds. J.-C. Vial, & O. Engvold, 415, 355
Mackay, D. H., Gaizauskas, V., & Yeates, A. R. 2008, Sol. Phys., 248, 51
Mackay, D. H., Karpen, J. T., Ballester, J. L., Schmieder, B., & Aulanier, G. 2010, Space Sci. Res., 151, 333
Martin, S. F. 1998, Sol. Phys., 182, 107
Martin, S. F., Livi, S. H. B., & Wang, J. 1985, Aust. J. Phys., 38, 929
Martin, S. F., Marquette, W. H., & Bilimoria, R. 1992, in The Solar Cycle, ed. K. L. Harvey, ASP Conf. Ser., 27, 53
Moore, R. L., & Labonte, B. J. 1980, in Solar and Interplanetary Dynamics, eds. M. Dryer, & E. Tandberg-Hanssen, 91, 207
Moore, R. L., Sterling, A. C., Hudson, H. S., & Lemen, J. R. 2001, ApJ, 552, 833
Okamoto, T. J., Tsuneta, S., Lites, B. W., et al. 2008, ApJ, 673, L215
Okamoto, T. J., Tsuneta, S., Lites, B. W., et al. 2009, ApJ, 697, 913
Ouyang, Y., Zhou, Y. H., Chen, P. F., & Fang, C. 2017, ApJ, 835, 94
Patsourakos, S., Vourlidas, A., & Stenborg, G. 2013, ApJ, 764, 125
Patsourakos, S., Vourlidas, A., Török, T., et al. 2020, Space Sci. Res., 216, 131
Pesnell, W. D., Thompson, B. J., & Chamberlin, P. C. 2012, Sol. Phys., 275, 3
Priest, E. R., & Démoulin, P. 1995, J. Geophys. Res., 100, 23443
Priest, E. R., Chitta, L. P., & Syntelis, P. 2018, ApJ, 862, L24
Qiu, Y., Guo, Y., Ding, M., & Zhong, Z. 2020, ApJ, 901, 13
Scherrer, P. H., Schou, J., Bush, R. I., et al. 2012, Sol. Phys., 275, 207
Schou, J., Scherrer, P. H., Bush, R. I., et al. 2012, Sol. Phys., 275, 229
Schuck, P. W. 2008, ApJ, 683, 1134
Syntelis, P., Archontis, V., & Tsinganos, K. 2017, ApJ, 850, 95
Tandberg-Hanssen, E. 1974, Solar Prominences, 12
Tandberg-Hanssen, E. 1995, The Nature of Solar Prominences, 199
Titov, V. S., Downs, C., Mikić, Z., et al. 2018, ApJ, 852, L21
Titov, V. S., Hornig, G., & Démoulin, P. 2002, J. Geophys. Res. (Space Phys.), 107, 1164
Titov, V. S., Török, T., Mikic, Z., & Linker, J. A. 2014, ApJ, 790, 163
Toriumi, S., & Takasao, S. 2017, ApJ, 850, 39
Török, T., Berger, M. A., & Kliem, B. 2010, A&A, 516, A49
van Ballegooijen, A. A., & Martens, P. C. H. 1989, ApJ, 343, 971
van Ballegooijen, A. A., Priest, E. R., & Mackay, D. H. 2000, ApJ, 539, 983
Vargas Domínguez, S., MacTaggart, D., Green, L., van Driel-Gesztelyi, L., & Hood, A. W. 2012, Sol. Phys., 278, 33
Wang, Y. M., & Muglach, K. 2007, ApJ, 666, 1284
Wang, Y. M., & Stenborg, G. 2010, ApJ, 719, L181
Wang, J., Shi, Z., & Martin, S. F. 1996, A&A, 316, 201
Wang, H., Cao, W., Liu, C., et al. 2015, Nat. Commun., 6, 7008
Wiegelmann, T., & Sakurai, T. 2012, Liv. Rev. Sol. Phys., 9, 5
Wiegelmann, T., Inhester, B., & Sakurai, T. 2006, Sol. Phys., 233, 215
Xing, C., Cheng, X., & Ding, M. D. 2020, The Innovation, 1
Yan, Y., Deng, Y., Karlický, M., et al. 2001, ApJ, 551, L115
Yan, X. L., Xue, Z. K., Pan, G. M., et al. 2015, ApJS, 219, 17
Yan, X., Li, Q., Chen, G., et al. 2020a, ApJ, 904, 15
Yan, X., Liu, Z., Zhang, J., & Xu, Z. 2020b, Sci. China E: Technol. Sci., 63, 1656
Yan, X., Xue, Z., Cheng, X., et al. 2020c, ApJ, 889, 106
Yan, X., Wang, J., Guo, Q., et al. 2021, ApJ, 919, 34
Yang, B., Jiang, Y., Yang, J., Yu, S., & Xu, Z. 2016a, ApJ, 816, 41
Yang, K., Guo, Y., & Ding, M. D. 2016b, ApJ, 824, 148
Yang, L., Yan, X., Xue, Z., et al. 2019, ApJ, 887, 239
Zhang, J., Cheng, X., & Ding, M.-D. 2012, Nat. Commun., 3, 747
Zhang, Q., Liu, R., Wang, Y., et al. 2014, ApJ, 789, 133
Zhong, Z., Guo, Y., Ding, M. D., Fang, C., & Hao, Q. 2019, ApJ, 871, 105
Zhu, X., Wang, H., Du, Z., & He, H. 2016, ApJ, 826, 51
Zou, P., Fang, C., Chen, P. F., et al. 2016, ApJ, 831, 123
Zou, P., Fang, C., Chen, P. F., Yang, K., & Cao, W. 2017, ApJ, 836, 122